Revisiting the maximum mass of differentially rotating neutron stars in general relativity with realistic equations of state

Pedro L. Espino[1] and Vasileios Paschalidis[1,2]

[1]*Department of Physics, University of Arizona, Tucson, Arizona 85721, USA*
[2]*Department of Astronomy, University of Arizona, Tucson, Arizona 85721, USA*

We study the solution space of general relativistic, axisymmetric, equilibria of differentially rotating neutron stars with realistic, nuclear equations of state. We find that different types of stars, which were identified by earlier works for polytropic equations of state, arise for realistic equations of state, too. Scanning the solution space for the sample of realistic equations of state we treat, we find lower limits on the maximum rest masses supported by cold, differentially rotating stars for each type of stars. We often discover equilibrium configurations that can support more than 2 times the mass of a static star. We call these equilibria "overmassive," and in our survey we find overmassive stars that can support up to 2.5 times the maximum rest mass that can be supported by a cold, nonrotating star with the same equation of state. This is nearly 2 times larger than what previous studies employing realistic equations of state had found, and which did not uncover overmassive neutron stars. Moreover, we find that the increase in the maximum rest mass with respect to the nonspinning stellar counterpart is larger for moderately stiff equations of state. These results may have implications for the lifetime and the gravitational wave and electromagnetic counterparts of hypermassive neutron stars formed following binary neutron star mergers.

I. INTRODUCTION

Hypermassive neutron stars (HMNSs) [1] are transient configurations that are supported against gravitational collapse by the additional centrifugal support provided by differential rotation, and possibly also by thermal pressure [2,3]. HMNSs may be ubiquitous remnants of binary neutron star (BNS) mergers (see, e.g., [4–7] for reviews and references therein). An HMNS was also a likely outcome [8–11] of the LIGO/Virgo event GW170817 [12,13].

The study of differentially rotating relativistic stars is useful for understanding the types of BNS merger remnants that are possible and their properties. Modest to high degrees of differential rotation may support an HMNS against collapse on dynamical timescales, but such objects are unstable on secular timescales (see, e.g., [3,14,15] and references therein). An important quantity that determines whether following a BNS merger there will be prompt, delayed, or no collapse at all is the maximum mass that can be supported given an equation of state. Studying general relativistic, equilibrium models of differentially rotating stars provides a straightforward approach to determine this maximum mass.

In [16,17] it was shown that cold, axisymmetric, differentially rotating stars described by either polytropic or realistic equations of state (EOSs) can support up to approximately 70% more mass when compared to the maximum rest mass that can be supported by a nonrotating star—the Tolman-Oppenheimer-Volkoff (TOV) limit. This

result holds for the differential rotation law of Komatsu, Eriguchi, and Hachisu [18] (referred to as the KEH law). However, in [19] it was pointed out that early efforts to find the maximum rest mass of differentially rotating, axisymmetric configurations did not account for the full solution space with the KEH law. Subsequently, it was found in [20] that differentially rotating, axisymmetric, $\Gamma = 2$ polytropic models of neutron stars built with the KEH law can support up to ∼4 times the TOV limit at even modest degrees of differential rotation.

The solution space for relativistic, differentially rotating, axisymmetric stars with the KEH law has been shown to exhibit four types of equilibrium solutions [19] labeled A, B, C, and D. A careful scan among these types reveals that stars with quasitoroidal topology are those that tend to be the most massive. Each stellar configuration belonging to a solution type falls along a sequence characterized by a quadruplet of parameters consisting of the maximum energy density $\epsilon_{\max}$, the degree of differential rotation $\hat{A}^{-1}$, the ratio of polar to equatorial radius r_p/r_e, and the parameter $\hat{\beta}$ describing how close to the mass-shedding limit the configuration is. Note that the first three of the above parameters are needed to completely specify a configuration, yet the solution space requires four parameters to be described. The full solution space with the KEH law has been studied in great detail for polytropic EOSs of varying stiffness [21]. In [21] it was further shown that the existence of four types of solutions is a universal feature for

a range of polytropic indices $n \in [2/3, 2]$. Nevertheless, for $n = 1.5$ the authors did not report stars of Type B, C, or D. These results imply that the possible types of solutions may depend on the equation of state. This is important because neutron star EOSs are not described by a single polytropic index and different realistic nuclear equations of state have varying degrees of stiffness. While $n = 1.5$ does not correspond to models of neutron stars, a natural question arises by the work of [20,21]: do the different types of differentially rotating, axisymmetric stars arise for realistic nuclear EOSs? If they do arise, what is the maximum rest mass that can be supported by the different types of solutions when realistic nuclear EOSs are considered?

In this paper, we address these questions by considering the solution space for differentially rotating, axisymmetric stars built with the KEH law with realistic nuclear EOSs. We find that the different types of solutions identified in [19] arise even for realistic neutron star matter. As in [20,21] we find that many configurations can support a mass more than 2 times the TOV limit. Moreover, we find configurations that can support a rest mass more than 2 times the supramassive limit (the maximum mass that can be supported when allowing for maximal uniform rotation). We term configurations that can support a rest mass more than 2 times the TOV limit "overmassive." We propose a different name for these because overmassive neutron stars (OMNS) are not likely to arise in nature through quasi-circular mergers of binary neutron stars, as neutron stars in binaries are not observed to have high enough spins to support much more mass than the TOV limit. For instance, even for the fastest spinning known neutron star with a period of 1.5 ms the enhancement on the maximum supportable mass over the TOV limit is $O(1\%)$. Thus, if OMNSs form through astrophysical processes, in all likelihood it would have to be through some more exotic channel than binary mergers. While one could define overmassive stars as those that can support more than 2 times the supramassive limit mass, our current definition takes into consideration prior knowledge on neutron star properties based on decades of neutron star observations. For the sample of realistic EOSs we explore, in our scan of the solution space we find OMNSs that can support up to 2.5 times (150% more mass than) the corresponding TOV limit.

The remainder of this paper is organized as follows. In Sec. II we review basic equations and details pertaining to the solution space of differentially rotating stars built with the KEH law. In Sec. III we present the EOSs we treat here and their basic properties. In Sec. IV we describe our methods and reproduce some of the results presented in [20] for a $\Gamma = 2$ polytrope. Section V details our results, showing the solution space of differentially rotating stars with realistic nuclear EOSs along with the maximum rest mass models we found for each EOS we considered. We conclude in Sec. VI with a summary of our findings and a

discussion of future directions. Geometrized units, where $G = c = 1$, are adopted throughout, unless otherwise specified.

II. BASIC EQUATIONS AND TYPES OF DIFFERENTIALLY ROTATING STARS

The spacetime of stationary, axisymmetric, equilibrium rotating stars is described by the following line element in spherical polar coordinates (see, e.g., [22])

$$ds^2 = -e^{\gamma+\rho}dt^2 + e^{2\alpha}(dr^2 + r^2 d\theta^2)$$
$$+ e^{\gamma-\rho}r^2 \sin^2\theta(d\phi - \omega dt)^2, \qquad (1)$$

where the metric potentials γ, ρ, α, and ω are functions of r and θ only and are determined by the solution of the Einstein equations coupled to the hydrostationary equilibrium equation for perfect fluids (see, e.g., [7] for a review and other forms of the line element used in the literature). To close the system of equations an EOS and a differential rotation law are required.

Most studies of differentially rotating stars adopt the KEH rotation law [18], which is also called j-constant rotation law (see [7] for a summary of other differential rotation laws). In this law the specific angular momentum is a function of the angular velocity as follows:

$$u^t u_\phi = A^2(\Omega_c - \Omega), \qquad (2)$$

where u^t and u^ϕ are the temporal and azimuthal components of the fluid four velocity, respectively, $\Omega = u^\phi/u^t$ is the local angular velocity of the fluid as seen by an observer at infinity, and Ω_c is the angular velocity on the rotation axis. It is common and convenient to parametrize the angular velocity by considering the ratio of polar (r_p) to equatorial (r_e) radius of the star, $\frac{r_p}{r_e}$. Stars with larger values of Ω_c tend to have a smaller value of $\frac{r_p}{r_e}$, indicative of a "flatter" stellar shape. The parameter A in Eq. (2) has units of length and is a measure of the degree of differential rotation in the star, i.e., the length scale over which the fluid angular velocity changes in the star. It is also common to use a rescaled A parameter

$$\hat{A}^{-1} = \frac{r_e}{A}. \qquad (3)$$

A general relativistic stellar configuration is then completely determined by the values of $\hat{A}^{-1}$, $\frac{r_p}{r_e}$, and the central or maximum energy density (ϵ_{max}). In the case of uniform rotation or cases with low degrees of differential rotation the central energy density and ϵ_{max} coincide, since ϵ_{max} occurs at the center of the star. However, when considering differentially rotating stars a quasitoroidal topology may arise in which case ϵ_{max} is not at the geometric center of the configuration. In these cases it is more convenient to

specify $\epsilon_{\max}$ instead of the value of the energy density at the center of the star. Models with extreme quasitoroidal shapes tend to have very small (but nonzero) densities near the center.

The parameter $\hat{A}^{-1}$ is important for identifying the different types of solutions that arise for rotating stars. When $\hat{A}^{-1} = 0$ the stars are uniformly rotating, while stars with $\hat{A}^{-1} \neq 0$ are differentially rotating. Models with relatively high values of $\hat{A}^{-1}$ (typically $\hat{A}^{-1} \gtrsim 1.0$) tend to show a smooth transition from spheroidal to quasitoroidal topologies, depending on the values of $\frac{r_p}{r_e}$ and $\epsilon_{\max}$. Models with lower values of $\hat{A}^{-1}$ (typically $\hat{A}^{-1} \lesssim 0.7$ for the values of $\epsilon_{\max}$ considered here) show a richer solution space, as we discuss below.

Another important parameter in describing differentially rotating stars is β, which parametrizes how close to mass shedding the stellar model is. The parameter β was introduced in [19] and is defined as

$$\beta = -\left(\frac{r_e}{r_p}\right)^2 \frac{d(z^2)}{d(\varpi^2)}\bigg|_{\varpi = r_e}, \qquad (4)$$

where $\varpi = r \sin(\theta)$ and $z = r \cos(\theta)$ are cylindrical coordinates, and the derivative is evaluated on the surface of the star at the equator. On the surface of the star $r = r(\theta)$, and thus the function $z^2(\varpi^2)$ describes the surface shape, whose slope at the stellar equator determines how close to mass shedding the configuration is. The "mass-shedding parameter" is defined in terms of β as [19]

$$\hat{\beta} = \frac{\beta}{1 + \beta}. \qquad (5)$$

While $\hat{\beta}$ is not a gauge-invariant quantity, it is useful in describing models in coordinates such as those defined by Eq. (1). Depending on the surface slope at the equator, $\hat{\beta}$ will approach different values. We are generally interested in three limiting values of $\hat{\beta}$:

(1) Nonrotating, spherical limit: For a spherical TOV star, $\frac{r_p}{r_e} = 1$, and the derivative $\frac{d(z^2)}{d(\varpi^2)} = -1$ everywhere on the surface. Thus, in this limit $\hat{\beta} \to \frac{1}{2}$.

(2) Mass-shedding limit: At the mass-shedding limit, the stellar configuration begins to lose mass at the equator. The surface derivative at the equator vanishes $\frac{d(z^2)}{d(\varpi^2)} = 0$. Hence, $\hat{\beta} \to 0$ at the mass-shedding limit.

(3) Toroidal limit: As the stellar topology approaches that of a toroid, $r_p \to 0$, and β becomes large. This implies that $\hat{\beta} \to 1$ as a sequence approaches the toroidal limit.

The above discussion suggests that the complete set of parameters describing general relativistic equilibria of stationary and axisymmetric, differentially rotating stars with the KEH law is the quadruplet $(\epsilon_{\max}, \frac{r_p}{r_e}, \hat{A}^{-1}, \hat{\beta})$.

The solution types can be distinguished by specifying $\epsilon_{\max}$ and considering the limiting values of $\hat{\beta}$ for sequences of constant $\hat{A}^{-1}$ in the $(\frac{r_p}{r_e}, \hat{\beta})$ plane. This requires that one slowly vary the quadruplet $(\epsilon_{\max}, \frac{r_p}{r_e}, \hat{A}^{-1}, \hat{\beta})$ to carefully scan the space of solutions. We use the convention introduced in [19] to distinguish the types of differentially rotating stars at fixed $\epsilon_{\max}$ for sequences of constant $\hat{A}^{-1}$. Given that in the numerical construction of rotating stars we always start with an initial guess solution corresponding to a static star, and then slowly vary the stellar parameters to reach a particular type of solution at fixed $\epsilon_{\max}$, below we list the general trajectory of solutions used in building the corresponding sequences:

(i) Type A: This sequence of solutions consists strictly of spheroids. For low degrees of differential rotation (i.e., close to rigid rotation), stars are spheroidal. Spinning these stars up (i.e., decreasing $\frac{r_p}{r_e}$) results in mass shedding, so that the Type A sequence goes from the limiting solution of spherical stars ($\frac{r_p}{r_e} = 1, \hat{\beta} = 0.5$) to mass shedding ($\hat{\beta} = 0$). Starting from a spherical solution, these models are obtained by simply spinning up the initial model. A potential path in the parameter space is as follows:

Spheroid (low $\hat{A}^{-1}$) $\xrightarrow{\text{decrease} \frac{r_p}{r_e}}$ Mass shedding.

(ii) Type B: This type of star often exists for the same values of $\hat{A}^{-1}$ as Type A stars, but at lower values of $\frac{r_p}{r_e}$. Spinning these stars down (increasing $\frac{r_p}{r_e}$) results eventually in mass shedding. Therefore, the Type B sequence goes from the limiting solution of toroids ($\hat{\beta} \to 1.0$) to mass shedding ($\hat{\beta} = 0$). These models can be reached numerically by spinning up an initial spherical model (decreasing $\frac{r_p}{r_e}$) with high $\hat{A}^{-1}$ to obtain quasitoroidal solutions, then decreasing $\hat{A}^{-1}$, and finally increasing $\frac{r_p}{r_e}$ to approach the mass-shedding limit. A potential path in the parameter space is as follows:

Spheroid (low $\hat{A}^{-1}$) $\xrightarrow{\text{increase} \hat{A}^{-1}, \text{decrease} \frac{r_p}{r_e}}$ Quasitoroid (high $\hat{A}^{-1}$) $\xrightarrow{\text{decrease} \hat{A}^{-1}}$ Quasitoroid (low $\hat{A}^{-1}$) $\xrightarrow{\text{increase} \frac{r_p}{r_e}}$ Mass shedding.

The Type B stars near the mass-shedding limit are difficult to reach, and we were not able to construct such extreme configurations.

(iii) Type C: This sequence exhibits a smooth transition from a spherical solution ($\hat{\beta} = 0.5$) to a quasitoroidal solution ($\hat{\beta} = 1.0$). As such, starting at a spheroid with high $\hat{A}^{-1}$ and spinning Type C stars up by decreasing $\frac{r_p}{r_e}$ would not result in mass

shedding, but would shape the models into a quasitoroid. A potential path in the parameter space is as follows:

$$\text{Spheroid} \quad (\text{low} \quad \hat{A}^{-1}) \xrightarrow[\text{decrease } \frac{r_p}{r_e}]{\text{increase } \hat{A}^{-1}} \quad \text{Quasitoroid}$$

(high $\hat{A}^{-1}$).

(iv) Type D: This type typically covers the smallest part of the parameter space. The models of this type are nontrivial to build directly from a spherical solution. This is because Type D sequences start and end at the mass-shedding limit ($\hat{\beta} = 0$). Spinning these stars either up or down would result in mass shedding. We were unable to build Type D sequences at fixed values of $\hat{A}^{-1}$ for any of the cases considered. However, we were able to construct individual *candidate* Type D models at specific values of the quadruplet ($\epsilon_{\max}, \frac{r_p}{r_e}, \hat{A}^{-1}, \hat{\beta}$).

III. EQUATIONS OF STATE

We consider a set of four realistic EOSs, all of which can be found on the Compstar Online Supernovae Equations of State (ComPOSE) [23] database. We chose two zero-temperature EOSs and two finite temperature EOSs (in their "cold" limit) to study. The zero-temperature, nuclear EOSs we considered are APR [24] and FPS [25]. These zero-temperature EOSs were also considered in [17] and were chosen for a suitable comparison to the maximum rest mass models found therein.

The first finite temperature EOS we consider is a variant of the EOS of [26], which includes electrons, protons, and neutrons and will hereafter be referred to as NL3. We also consider the EOS of [27], will hereafter be referred to as HFO (a common name for the HFO EOS in the existing literature is SFHO). The finite temperature EOS tables include values of the rest mass density ρ_0 at different values of the temperature T and the electron fraction Y_e. Since our focus is on cold, equilibrium models of differentially rotating stars we set $T = 0.01$ MeV, and enforce neutrino-less beta equilibrium as is common in the case of finite temperature EOSs. In particular, we numerically solve for the value of Y_e at which chemical equilibrium is established between neutrons, protons, and electrons,

$$\mu_n - \mu_p - \mu_e = 0, \tag{6}$$

where μ_i is the chemical potential of species i. Once ρ_0 and T are specified for the EOS tables, we scan through values of Y_e until the condition in Eq. (6) is met. We then change the value of ρ_0 and repeat, building a tabulated EOS of pressure, rest mass density, and energy density for the set of electron fractions corresponding to beta equilibrium. Figure 1 shows a plot of pressure as a function of energy density for the set of EOSs we treat in this work. We discuss
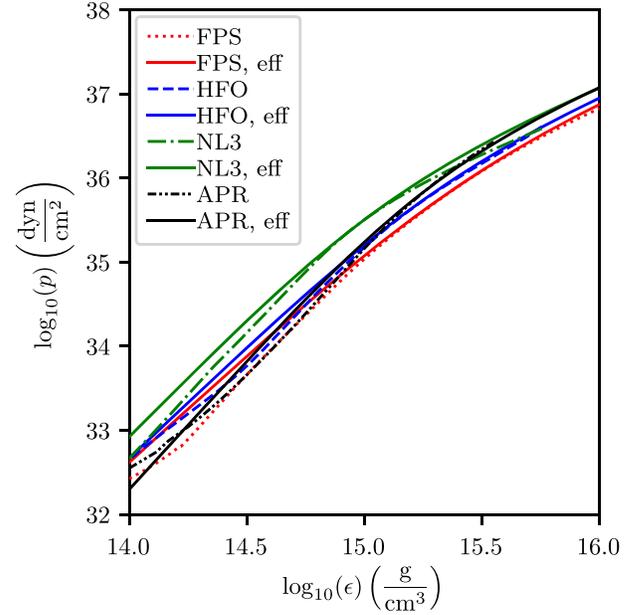
FIG. 1. Pressure as a function of energy density for the EOSs in our sample. The red dashed, blue dotted, green dash-dotted, and black dashed–double-dotted lines correspond to the FPS, HFO, NL3, and APR EOSs, respectively. The solid lines of the same color scheme correspond to representations of each EOS using a single polytrope as described by Eqs. (A3) and (A4).

the relevant astrophysical bounds for these EOSs in Appendix C.

We compare the EOSs in terms of their stiffness, which we characterize by the ratio of average energy density $\bar{\epsilon}$ to maximum energy density $\epsilon_{\max}$ in models of equal rest mass M_0 for each EOS. The average density is defined as [17]

$$\bar{\epsilon} \equiv \frac{3M}{4\pi R_c^3}, \tag{7}$$

where M is the gravitational mass (also referred to as the Arnowitt Deser Misner, or ADM, mass M_{ADM}) and R_c the circumferential radius. We build $M_0 = 1.4\ M_\odot$ TOV models for each EOS and look at the ratio of average to maximum energy density C_ϵ,

$$C_\epsilon = \frac{\bar{\epsilon}}{\epsilon_{\max}}. \tag{8}$$

A maximally stiff EOS would have $C_\epsilon = 1$, corresponding to a uniform energy density configuration. We list $C_\epsilon^{1.4}$ [Eq. (8) for a 1.4 $M_\odot$ star] for each EOS in Table I. Using C_ϵ as a measure for stiffness is accurate for polytropic equations of state, because a larger adiabatic index yields larger C_ϵ for fixed mass. However, since C_ϵ varies with rest mass (see Appendix B), it is important to use additional measures of stiffness for realistic EOSs.

As an alternative measure of EOS stiffness, and to compare with the polytropic models in [20], we also

TABLE I. Ratio of average energy density to maximum energy density $C_\epsilon^{1.4}$ (for models of rest mass $M_0 = 1.4\,M_\odot$) and effective adiabatic index $\Gamma_{\text{eff}}^{\text{nuc}}$ as measures of EOS stiffness for each EOS in our study. $M_{0,\text{max}}^{\text{TOV}}$ and $M_{0,\text{max}}^{\text{sup}}$ are the rest masses of the TOV limit and the supramassive limit, respectively, and $M_{\text{ADM,max}}^{\text{TOV}}$ and $M_{\text{ADM,max}}^{\text{sup}}$ are the gravitational masses of the TOV limit and the supramassive limit, respectively. All masses are in units of $M_\odot$.

EOS	$C_\epsilon^{1.4}$	$\Gamma_{\text{eff}}^{\text{nuc}}$	$M_{0,\text{max}}^{\text{TOV}}$	$M_{0,\text{max}}^{\text{sup}}$	$M_{\text{ADM,max}}^{\text{TOV}}$	$M_{\text{ADM,max}}^{\text{sup}}$
FPS	0.40	2.55	2.10	2.45	1.80	2.12
HFO	0.42	2.66	2.41	2.83	2.06	2.44
NL3	0.43	2.84	3.27	3.88	2.75	3.30
APR	0.44	3.07	2.66	3.09	2.19	2.60

consider the effective adiabatic index $\Gamma_{\text{eff}}^{\text{nuc}}$ for each model, calculated as in [17]. In particular, to find $\Gamma_{\text{eff}}^{\text{nuc}}$ for each realistic EOSs we first calculate C_ϵ^{nuc} for the maximum rest mass TOV model. Next, we calculate the ratio C_ϵ^{poly} for the maximum rest mass TOV models of polytropes with a wide range of adiabatic indices Γ^{poly} and construct a function $\Gamma^{\text{poly}}(C_\epsilon^{\text{poly}})$ that we linearly interpolate over the range of C_ϵ^{poly} considered. The effective adiabatic index of a nuclear EOS is then defined through

$$\Gamma_{\text{eff}}^{\text{nuc}} = \Gamma^{\text{poly}}(C_\epsilon^{\text{nuc}}). \tag{9}$$

$\Gamma_{\text{eff}}^{\text{nuc}}$ is an "average" rate of change of pressure with rest-mass density by approximating the EOS as a single polytrope in the high density regime that primarily determines the bulk structure of the star. $\Gamma_{\text{eff}}^{\text{nuc}}$ is useful when comparing features in the solution space of realistic EOSs to those of polytropes. All of the EOSs in our set have $2.5 < \Gamma_{\text{eff}}^{\text{nuc}} < 3.1$, and it turns out that certain features of the solution space for these realistic EOSs are consistent with the $\Gamma \geq 2.5$ polytropes [21], as further discussed in Sec. V.

The effective adiabatic indices for the EOSs we treat are listed in Table I, where we also show the TOV limit mass and the supramassive limit mass for each of these EOSs. Compared to the values of $\Gamma_{\text{eff}}^{\text{nuc}}$ reported in [17] for the FPS and APR EOSs, our results differ by 0.04% and 1.56%, respectively. Note that we have ranked the EOSs in Table I in order of increasing $C_\epsilon^{1.4}$ and $\Gamma_{\text{eff}}^{\text{nuc}}$. By both metrics of the stiffness APR is the stiffest, and FPS is the softest.

In order to see how well approximated the realistic EOSs are by single polytropes, we also include a polytropic representation of each nuclear EOS. Along with the effective adiabatic index $\Gamma_{\text{eff}}^{\text{nuc}}$, we calculate an effective polytropic constant $\kappa_{\text{eff}}^{\text{nuc}}$ for each EOS as detailed in Appendix A.

The polytropic representations of the nuclear EOSs are presented in Fig. 1. Although not perfect, using a single polytrope to represent the nuclear EOS is reasonable at higher densities, and the qualitative results of [21] for

polytropes of varying polytropic indices may be suitably compared to those presented in this work for nuclear EOSs.

IV. METHODS

We adopt the code detailed in [22,28] (hereafter referred to as the Cook code) to solve the coupled Einstein-hydro-stationary equilibrium equations in axisymmetry. This code was also used in [16,17]. In this section we describe the numerical grid and tests we performed to validate the code in the case of differentially rotating stars found by [19–21].

A. Numerical grid and determination of stellar surface

The stellar models are constructed on a numerical grid where the computational domain in spherical polar coordinates covers the regions $0 \leq r \leq \infty$ and $0 \leq \theta \leq 2\pi$. Instead of the coordinates (r, θ) in Eq. (1), the code solves the coupled Einstein-hydrostationary equations in coordinates defined by $u = \cos\theta$ and a compactified radial coordinate s that maps spatial infinity onto the computational domain as

$$r \equiv r_e\left(\frac{s}{1-s}\right). \tag{10}$$

By construction, the surface of the star on the equator corresponds to $r \to r_e$ and $s \to \frac{1}{2}$.

Adopting the coordinates (u, s) results in the radial grid points being concentrated closer to the origin. This is not very convenient, because it does not allow an accurate determination of the stellar surface, which is necessary to compute $\hat{\beta}$ through the surface derivative appearing in Eq. (4). To resolve this problem we adopt very high radial resolution. We use linear interpolation along r of the pressure (p) to determine the location where the pressure drops to 10^{10} dyn/cm^2, which is more than 20 orders of magnitude below the maximum pressure in the neutron star models. We call that location the surface of the star. We have experimented with higher order interpolation, too, but found that linear interpolation exhibits convergence to within 1% in most cases, and within 3% at most in some cases, in finding the surface at the adopted radial resolutions. This is not the case with higher order interpolation because it is oscillatory. This procedure determines the surface of the star as $r_{\text{surf}}(u)$, which we use to compute numerically the derivative needed for $\hat{\beta}$ in Eq. (4), which we reexpress as

$$\hat{\beta} = -\left(\frac{r_e}{r_p}\right)^2 \left(\frac{\frac{dz^2}{du^2}}{\frac{d\varpi^2}{du^2}}\right)_{r_e}, \tag{11}$$

where

$$z^2 = [r_{\text{surf}}(u)]^2 u^2 \tag{12}$$

and

$$\varpi^2 = [r_{\mathrm{surf}}(u)]^2(1-u^2). \qquad (13)$$

We use a three-point one-sided stencil for finite differencing combined with high radial resolution on the solution grid to determine the numerical derivatives in Eq. (11). We determine the necessary grid resolution by calculating $\hat{\beta}$ for benchmark sequences including spheroidal, quasitoroidal, and near mass-shedding models at increasing resolution until the results converge to within 1% accuracy in most cases, but within 3% at most in some cases. A typical configuration is constructed with 500 grid points covering the equatorial radius for polytropes, 1250 points covering the equatorial radius for nuclear EOSs, and 500 grid points covering the angular direction in all cases. All parameters in the quadruplet $(\epsilon_{\max}, \frac{r_p}{r_e}, \hat{A}^{-1}, \hat{\beta})$ besides $\hat{\beta}$ are specified as inputs to the Cook code.

B. Solution space of a $\Gamma = 2$ polytrope

A polytropic EOS is described by

$$p = \kappa \rho_0^{\Gamma}, \qquad (14)$$

where p is the pressure, ρ_0 is the rest mass energy density, κ is the polytropic constant, and Γ is the adiabatic index. When treating polytropes, we employ polytropic units, such that $\kappa = G = c = 1$. For a $\Gamma = 2$ polytrope, Refs. [19,20] showed that there exist four types of solutions, as we discussed in Sec. II, and focused on the maximum rest mass models obtainable for each type of solution. In [20] it was speculated that [16] was unable to discover the different types of solutions of differentially rotating stars due to limitations of the Cook code. Here we demonstrate that the Cook code can reproduce many of the $\Gamma = 2$ results reported in [20]. We find that how one searches the parameter space is the greatest limitation in constructing different types of differentially rotating stars. Given that the code of [20] is spectral, we use the results reported in that work to gauge the accuracy of the Cook code.

Unlike the code of [20], which employs surface fitted grids and also appears to be able to control the parameter $\hat{\beta}$, the Cook code builds rotating stars by specifying the triplet $(\epsilon_{\max}, \frac{r_p}{r_e}, \hat{A}^{-1})$. Once a configuration has been built, $\hat{\beta}$ is determined by the use of Eq. (11). This makes scanning the full parameter space challenging and is probably the reason why we were not able to build sequences of Type D and lower-$\hat{\beta}$ Type B stars.

At a given value of $\epsilon_{\max}$, there exists a critical degree of differential rotation at which the solution space exhibits equilibrium solutions of all types (A, B, C, and D). Three out of the four solution types we were able to construct with the Cook code for $\epsilon_{\max} = 0.12$ are shown in Fig. 2.
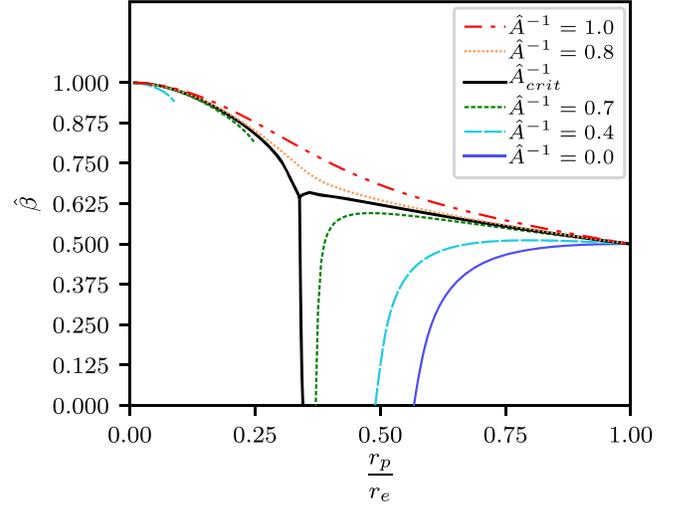
FIG. 2. Mass-shedding parameter $\hat{\beta}$ as a function of $\frac{r_p}{r_e}$ at fixed maximum energy density $\epsilon_{\max} = 0.12$ for a $\Gamma = 2$ polytrope at varying degrees of differential rotation. The solid black line shows the separatrix at the critical value of differential rotation $\hat{A}_{\mathrm{crit}}^{-1} = 0.75904$ found in [19], which divides the solution space into the three regions wherein we are able to build equilibrium models. The colored lines show the characteristic sequences of equilibrium models for spheroids (Type A, right of the separatrix), quasitoroids (Type B, left of the separatrix), and spheroids/quasitoroids (Type C, above the separatrix).

The solid black curve in the plot is the separatrix in the solution space that corresponds to the critical degree of differential rotation and separates the space into four regions, each corresponding to a solution type (although here we have only three regions because we could not generate Type D sequences). Type A solutions are found on the lower right part of the plot, e.g., with values of $\hat{A}^{-1} \in \{0.0, 0.4, 0.7\}$; Type B solutions are found on the left side of the plot, e.g., with values of $\hat{A}^{-1} \in \{0.4, 0.7\}$; and Type C solutions are found along the top part of the plot, e.g., with values of $\hat{A}^{-1} \in \{0.8, 1.0\}$.

C. Solution space

It was shown in [19] that for a fixed value of $\epsilon_{\max}$, $\hat{A}^{-1}$ is a function of $\frac{r_p}{r_e}$ and $\hat{\beta}$ exhibits a saddle point at the value $\hat{A}^{-1} = \hat{A}_{\mathrm{crit}}^{-1}$, so that the solution to the equations

$$\left(\frac{\partial \hat{A}^{-1}}{\partial(r_p/r_e)}\right)_{\epsilon_{\max}} = 0 = \left(\frac{\partial \hat{A}^{-1}}{\partial \hat{\beta}}\right)_{\epsilon_{\max}} \qquad (15)$$

defines the value $\hat{A}_{\mathrm{crit}}^{-1}$. Instead of solving these equations we use a different method to find the critical degree of differential rotation. For each $\frac{r_p}{r_e}$ and at fixed $\epsilon_{\max}$, there exists a minimum value of $\hat{A}^{-1}$ for which equilibrium solutions exist. We denote this minimum value $\hat{A}_{\min}^{-1}$.

TABLE II. Critical degree of differential rotation $\hat{A}_{crit}^{-1}$ at several values of the maximum energy density ϵ_{max} [and log of specific enthalpy $H_{max} \equiv \log(h_{max})$] in polytropic units for polytropes of four different polytropic indices Γ. Also shown is the percent error [calculated using (17)] for each value of $\hat{A}_{crit}^{-1}$ compared with those of Table A1 in [21].

Γ	ϵ_{max}	H_{max}	$\hat{A}_{crit}^{-1}$	$\delta(\hat{A}_{crit}^{-1})$
1.8	0.023	0.1	1.016	0.294
2.0	0.123	0.2	0.758	0.132
2.5	0.402	0.3	0.480	0.629
3.0	0.667	0.4	0.340	0.295

The function $\hat{A}_{min}^{-1}(\frac{r_p}{r_e})$ exhibits a maximum, and the maximum value is $\hat{A}_{crit}^{-1}$. We effectively solve Eq. (15) by locating the maximum in the $(\frac{r_p}{r_e}, \hat{A}_{min}^{-1})$ plane. We find that this extremum is a *global* maximum, so that it is possible to accurately locate the value of $\hat{A}_{crit}^{-1}$ with our method instead of actually solving Eq. (15) as was done in [20]. The critical value we find for $\Gamma = 2$ polytropes at $\epsilon_{max} = 0.12$ is $\hat{A}_{crit}^{-1} = 0.7612$, which is only ~0.284% greater than the critical value of $\hat{A}_{crit}^{-1} = 0.75904$ found in [20]. To more accurately determine the value of $\hat{A}_{crit}^{-1}$ we slowly lower the value of $\hat{A}^{-1}$ until we reach a value that exhibits solutions of all types (except for Type D, which we cannot build), which are continuously joined (the defining feature of the sepa-ratrix). This procedure allows for the determination of $\hat{A}_{crit}^{-1}$ to better than 1% accuracy. In Table II we show the value of $\hat{A}_{crit}^{-1}$ found using our method for polytropes across several

polytropic indices and values of the maximum energy density. Values of $\hat{A}_{crit}^{-1}$ at the same maximum energy densities and for the same polytropic indices can be found in Table A1 in [21]. All of the values of $\hat{A}_{crit}^{-1}$ presented in Table II agree with those in Table A1 in [21] to within 1%. Note that we also list the logarithm of the specific enthalpy $H_{max} \equiv \log(h_{max})$, where

$$h = \frac{\epsilon + p}{\rho_0}, \qquad (16)$$

to offer easier comparison to the results of [21].

In Table III we show properties of the maximum rest mass models obtained for a $\Gamma = 2$ polytrope. For each quantity also computed in [20], we show the percent error between our models and the corresponding ones in [20], computed as

$$\delta x \equiv \frac{|x - x_{ref}|}{x_{ref}} \times 100, \qquad (17)$$

where x represents the values obtained using the Cook code and x_{ref} represents the values presented in [20]. Given that the code of [20] is spectral, δx is an estimate of the error in our calculations for the resolution we adopt. Note that we also show δx for the values of $\hat{A}_{crit}^{-1}$ in Table II.

The highest fractional differences are seen in the Type B models, going as high as $\mathcal{O}(10\%)$ in the rest mass and angular momentum for the most massive configuration and less than 10% in other quantities; in all other cases the errors are subpercent. We suspect that the relatively high

TABLE III. Listed are the degree of differential rotation $\hat{A}^{-1}$, ratio of polar to equatorial radius $\frac{r_p}{r_e}$, and maximum energy density ϵ_{max} for the maximum rest mass models of a $\Gamma = 2$ polytrope. Also shown for each model are the ratio of central to equatorial angular velocity $\frac{\Omega_c}{\Omega_e}$, the rest mass M_0, the ratio of kinetic to potential energy $\frac{T}{|W|}$, angular momentum J, and the ratio of ADM mass to circumferential radius $\frac{M}{R_c}$. For each quantity of interest we also report the percent error [$\delta()$] as defined in Eq. (17).

Type	$\hat{A}^{-1}$	$\frac{r_p}{r_e}$	ϵ_{max}	$\frac{\Omega_c}{\Omega_e}$	$\delta(\frac{\Omega_c}{\Omega_e})$	M_0	δM_0	$\frac{T}{|W|}$	$\delta(\frac{T}{|W|})$	J	δJ	$\frac{M}{R_c}$	$\delta(\frac{M}{R_c})$
A	0.0	0.585	0.350	1.000	0.000	0.207	0.029	0.083	0.240	0.020	0.843	0.174	0.155
	0.1	0.580	0.349	1.027	0.000	0.208	0.037	0.086	0.467	0.021	1.597	0.174	0.040
	0.2	0.565	0.347	1.108	0.000	0.211	0.037	0.093	0.432	0.022	0.677	0.174	0.275
	0.3	0.541	0.343	1.240	0.000	0.216	0.055	0.104	0.192	0.025	1.215	0.176	0.245
	0.4	0.511	0.335	1.422	0.000	0.224	0.011	0.120	0.332	0.028	1.720	0.178	0.231
	0.5	0.473	0.323	1.657	0.000	0.236	0.183	0.142	0.070	0.034	0.176	0.181	0.121
	0.6	0.427	0.304	1.959	0.000	0.254	0.079	0.171	0.117	0.043	0.327	0.188	0.181
	0.7	0.352	0.306	2.518	0.439	0.294	0.396	0.222	0.090	0.062	0.689	0.221	3.107
B	0.4	0.035	0.089	1.774	0.616	0.682	5.409	0.331	1.488	0.381	9.716	0.280	3.704
	0.5	0.114	0.084	1.976	1.496	0.586	8.294	0.324	3.284	0.289	15.000	0.259	5.285
	0.6	0.144	0.081	2.196	1.215	0.516	9.632	0.313	5.438	0.227	18.051	0.242	9.009
	0.7	0.164	0.081	2.458	0.614	0.463	9.216	0.302	6.790	0.184	18.222	0.231	14.925
C	0.8	0.005	0.097	2.997	0.067	0.463	0.041	0.294	0.102	0.176	0.114	0.250	0.160
	0.9	0.002	0.100	3.388	0.177	0.434	0.099	0.285	0.140	0.152	0.393	0.246	0.408
	1.0	0.005	0.103	3.809	0.105	0.409	0.120	0.277	0.036	0.134	0.149	0.241	0.207
	1.5	0.010	0.121	6.431	0.171	0.326	0.031	0.238	0.042	0.079	0.894	0.228	0.220

residuals in some of the Type B models we built are due to the fact that the solutions presented in [20] are near the mass-shedding limit (highly pinched and quasitoroidal at low $\hat{\beta}$), whereas the corresponding models presented here belong to the part of the Type B sequence at higher values of $\hat{\beta}$. Close inspection of the Type B sequences in [20] shows that they are not always single valued in $\frac{r_p}{r_e}$, so that without the full solution space coordinates [i.e., the full quadruplet $(\epsilon_{\max}, \frac{r_p}{r_e}, \hat{A}^{-1}, \hat{\beta})$] two distinct models may be misidentified as the same equilibrium solution. Because only the triplet $(\epsilon_{\max}, \frac{r_p}{r_e}, \hat{A}^{-1})$ is presented in [20] for these maximum mass models, we cannot be sure that we are comparing the same two models. However, the confidence in our solutions is supported by the fact that the majority of other cases show subpercent residuals in all of the model properties.

The highest mass models built in [20,21] were of Type B with the lowest value of $\hat{A}^{-1}$ among those considered. We note that the maximum rest mass Type D models presented in [20,21] exceed neither the maximum rest mass Type B models nor Type C models in the rest mass in all cases where they could be built. We anticipate that this result holds true for realistic EOSs, too. Although we were unable to construct a suitable sequence of Type D models with the Cook code, Type D models are likely unphysical as pointed out in [21]. Despite the limitations of nonspectral codes, here we showed that the Cook code can generate Type A, B, and C models, and closely match the maximum-mass configurations for a $\Gamma = 2$ polytrope obtained with a spectral code. This result gives us confidence that the maximum-mass models we report for realistic EOSs in the next section are the true maximum-mass Type A and C modes and are very close to the true maximum-mass Type B models.
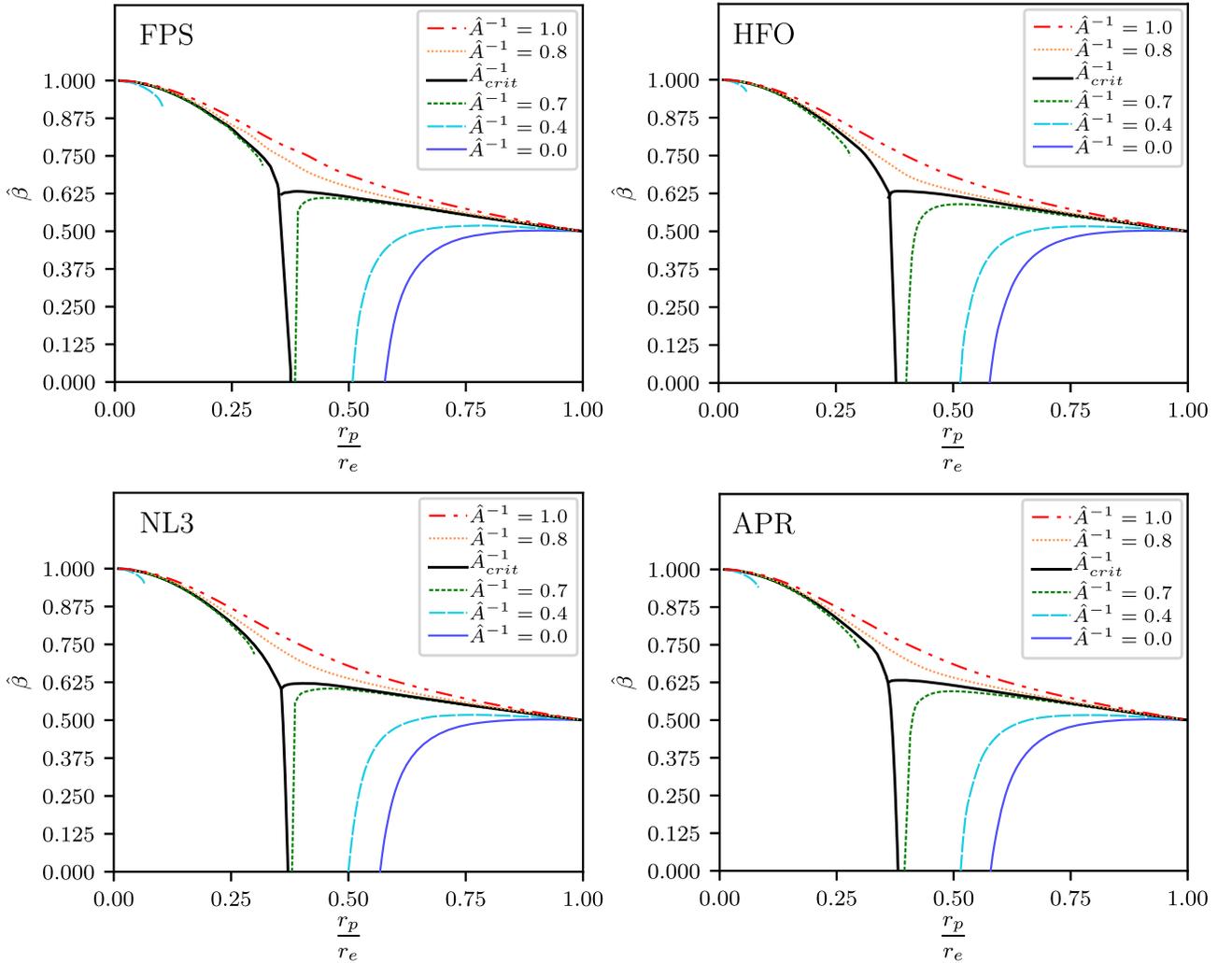
FIG. 3. Solution space for the FPS, HFO, NL3, and APR EOSs. These plots correspond to fixed energy densities, the values of which, along with $\hat{A}_{\text{crit}}^{-1}$, are displayed in Table IV for each EOS.

TABLE IV. Maximum energy density ϵ_{max} and corresponding critical degree of differential rotation $\hat{A}_{crit}^{-1}$ used in generating the solution spaces shown in Fig. 3 for realistic EOSs.

EOS	$\frac{\epsilon_{max}}{10^{15} \text{ g/cm}^3}$	$\hat{A}_{crit}^{-1}$
FPS	0.77	0.7161
HFO	0.6	0.753
NL3	0.35	0.717
APR	0.7	0.7376

V. RESULTS WITH REALISTIC EQUATIONS OF STATE

In this section we discuss the solution space of differentially rotating, relativistic stars with realistic equations of state and the maximum rest mass they can support.

The solution space depends on the value of ϵ_{max}. To reveal as large a fraction of the space of solutions as possible, for each EOS we obtain the critical degree of differential rotation $\hat{A}_{crit}^{-1}$ for different values of ϵ_{max}. Then we choose the values of ϵ_{max} for which $0.7 \leq \hat{A}_{crit}^{-1} \leq 0.8$. With this choice of ϵ_{max}, three out of four types of sequences we are able to construct are present for each of the EOSs considered. Moreover, models with $\hat{A}^{-1} \in [0.0, 0.4, 0.7]$ belong to sequences of Type A and B, and

models with $\hat{A}^{-1} \in [0.8, 1.0]$ belong to sequences of Type C. As in the $\Gamma = 2$ polytrope in the previous section, to scan the parameter space we fix the value of ϵ_{max}, modify the parameters $(\hat{A}^{-1}, \frac{r_p}{r_e})$ to construct stellar models and compute $\hat{\beta}$. Our results for the solution space of realistic EOSs with differential rotation at fixed ϵ_{max} are shown in Fig. 3. The values of ϵ_{max} and $\hat{A}_{crit}^{-1}$ for each EOS that correspond to Fig. 3 are given in Table IV. Figure 3 demonstrates that the existence of different types of differentially rotating stars are not a property of polytropic EOSs only. The different types exist for realistic EOSs, too.

In Fig. 4, we show meridional contours of the energy density ϵ normalized to ϵ_{max} for different types of differentially rotating stars constructed with the HFO EOS. The top left and right panels of Fig. 4 depict the maximum rest mass Type A models for $\hat{A}^{-1} = 0.0$ (uniform rotation) and $\hat{A}^{-1} = 0.4$ (largest rest mass Type A model), respectively. The bottom left and bottom right panels depict the largest rest mass Type B and Type C models, respectively.

Although we were not able to build complete sequences of Type D equilibria, we were able to construct individual *candidate* configurations near the mass-shedding limit, and for values of $\hat{A}^{-1} > \hat{A}_{crit}^{-1}$, all of which are properties of Type D models. For example, one candidate Type D configuration for the HFO EOS corresponds to
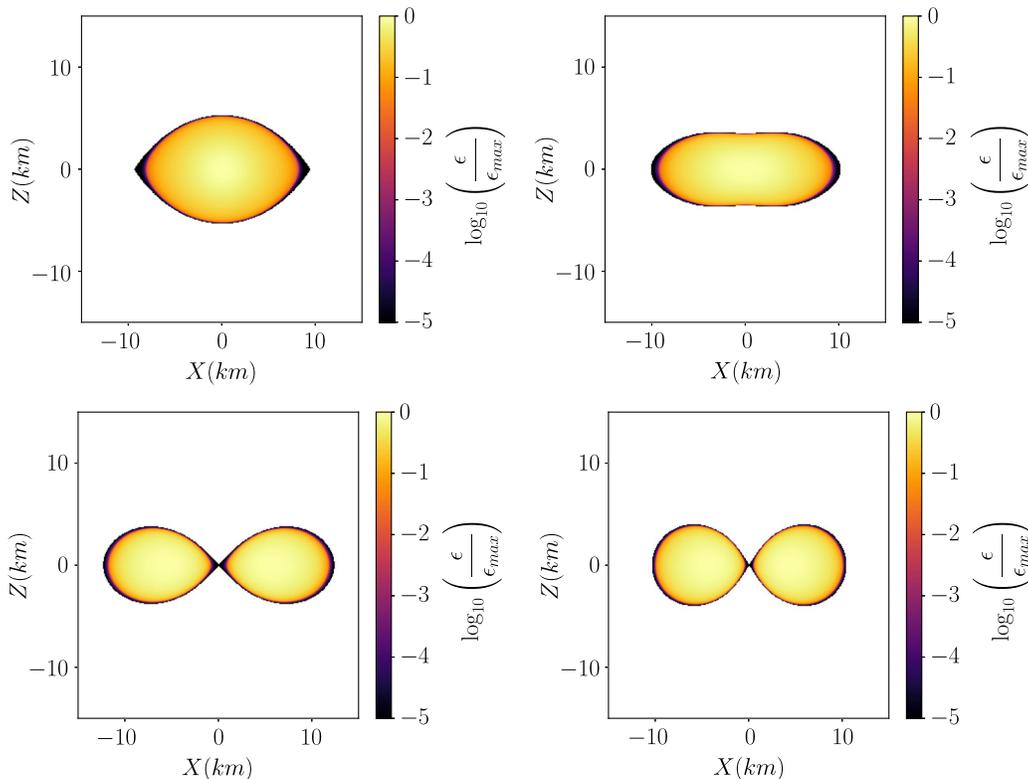
FIG. 4. Examples of meridional energy density contours for the HFO EOS. Top left: The maximum rest mass uniformly rotating ($\hat{A}^{-1} = 0.0$). Top right: The maximum rest mass Type A model. Bottom left: The maximum rest mass Type B model. Bottom right: The maximum rest mass Type C model.

$\epsilon_{\max} = 6 \times 10^{14}$ g/cm^3, $\frac{r_p}{r_e} = 0.375$, $\hat{A}^{-1} = 0.757$, and $\hat{\beta} = 0.064$. This candidate Type D model has $\frac{M_0}{M_{0,\max}^{\mathrm{TOV}}} = 0.574$ and $\frac{M_0}{M_{0,\max}^{\mathrm{sup}}} = 0.464$, meaning that they are less massive than the maximum rest mass TOV model of HFO. We were able to construct this model by finding a model close to mass shedding along the separatrix for the panel corresponding to HFO in Fig. 3 (i.e., using the values of $\epsilon_{\max}$ and $\hat{A}^{-1}$ from Table VI for HFO). Once the closest model to mass shedding for the separatrix was built, we decreased the value of $\frac{r_p}{r_e}$ while increasing the value of $\hat{A}^{-1}$ and searched for models near mass shedding.

A. Maximum rest mass

We search for the maximum rest mass models for $\hat{A}^{-1} \in [0.0, 1.0]$ in increments of 0.1, as well as for $\hat{A}^{-1} = 1.5$. We also build the benchmark TOV limit model ($M_{0,\max}^{\mathrm{TOV}}$), and the supramassive limit model ($M_{0,\max}^{\mathrm{sup}}$) against which we compare the increase in rest mass when considering differential rotation. For these same models, we also consider the increase in the gravitational mass compared to the gravitational mass of the TOV limit ($M_{\mathrm{ADM,max}}^{\mathrm{TOV}}$) and the supramassive limit ($M_{\mathrm{ADM,max}}^{\mathrm{sup}}$). As a reminder, the values for $M_{0,\max}^{\mathrm{TOV}}$, $M_{0,\max}^{\mathrm{sup}}$, $M_{\mathrm{ADM,max}}^{\mathrm{TOV}}$, and $M_{\mathrm{ADM,max}}^{\mathrm{sup}}$ for each EOS in our sample are shown in Table I. To find the maximum rest mass Type A and C models presented here

we built sequences of constant $\hat{A}^{-1}$ and $\epsilon_{\max}$ while varying $\frac{r_p}{r_e}$ from 1.0 to 0.01 and found the model with the largest rest mass. To find the maximum rest mass Type B models presented here we first built models at $\hat{A}^{-1} = 1.5$ and $\frac{r_p}{r_e} = 0.01$ (Type C models), then decreased $\hat{A}^{-1}$ to the target value, and finally increased $\frac{r_p}{r_e}$ to as high as possible. For each model type we then change the value of $\epsilon_{\max}$ while holding $\hat{A}^{-1}$ fixed and repeat the aforementioned scans, resulting in a set of maximum rest mass models for each value of $\epsilon_{\max}$ at a given value of $\hat{A}^{-1}$. The model with the largest rest mass among these is taken to be the maximum rest mass model for a given value of $\hat{A}^{-1}$ and of a given type (A, B, or C). We note that since we are not able to build complete $\hat{A}^{-1}$ − constant sequences for Type B stars, the values we report for the Type B stars correspond to the maximum rest mass configurations found in our search.

Properties of the maximum rest mass models are shown in Tables V–VIII. We also list whether a given maximum rest mass model is supramassive, hypermassive, or overmassive. We remind the reader that supramassive stars are uniformly rotating stars that can support more mass than the TOV limit. Hypermassive stars are those with masses that exceed the maximum mass that can be supported by supramassive stars (the supramassive limit). As such, hypermassive stars can only exist in cases with differential rotation. Overmassive stars are those with masses exceeding twice the TOV limit. We find that for the four EOSs

TABLE V. Maximum rest mass models for the FPS EOS. Shown are the values of the degree of differential rotation $\hat{A}^{-1}$, the maximum energy density $\epsilon_{\max}$ in units of $10^{15} \frac{\mathrm{g}}{\mathrm{cm}^3}$, the ratio of polar to equatorial radius $\frac{r_p}{r_e}$, the mass-shedding parameter $\hat{\beta}$, the circumferential radius R_c in units of km, the ratio of kinetic to gravitational potential energy $\frac{T}{|W|}$, the ratio of central to equatorial angular velocity $\frac{\Omega_c}{\Omega_e}$, the dimensionless spin $\frac{J}{M^2}$, the compactness $C = \frac{M_{\mathrm{ADM}}}{R_c}$, the rest mass M_0, the ratio of rest mass to the TOV limit rest mass $M_{0,\max}^{\mathrm{TOV}}$, the ratio of rest mass to the supramassive limit rest mass $M_{0,\max}^{\mathrm{sup}}$, and the ADM mass M_{ADM} along with the ratio of ADM mass to TOV limit ADM mass $M_{\mathrm{ADM,max}}^{\mathrm{TOV}}$ and the supramassive limit ADM mass $M_{\mathrm{ADM,max}}^{\mathrm{sup}}$. Also shown is the classification of each star as supramassive (SUP), hypermassive (HYP), or overmassive (OBE).

Type	$\hat{A}^{-1}$	$\epsilon_{\max}$	$\frac{r_p}{r_e}$	$\hat{\beta}$	R_c	$\frac{T}{\|W\|}$	$\frac{\Omega_c}{\Omega_e}$	$\frac{J}{M^2}$	C	$\frac{M_0}{M_\odot}$	$\frac{M_0}{M_{0,\max}^{\mathrm{TOV}}}$	$\frac{M_0}{M_{0,\max}^{\mathrm{sup}}}$	$\frac{M_{\mathrm{ADM}}}{M_\odot}$	$\frac{M_{\mathrm{ADM}}}{M_{\mathrm{ADM,max}}^{\mathrm{TOV}}}$	$\frac{M_{\mathrm{ADM}}}{M_{\mathrm{ADM,max}}^{\mathrm{sup}}}$	CLASS
A	0.0	2.92	0.568	0.060	12.44	0.117	1.000	0.658	0.170	2.452	1.167	1.000	2.120	1.178	1.000	SUP
	0.1	2.92	0.557	0.097	12.50	0.123	1.049	0.674	0.171	2.478	1.179	1.010	2.143	1.190	1.011	HYP
	0.2	2.90	0.526	0.202	12.69	0.141	1.194	0.719	0.174	2.557	1.217	1.043	2.213	1.230	1.044	HYP
	0.3	2.87	0.470	0.305	13.05	0.173	1.442	0.786	0.180	2.713	1.291	1.106	2.350	1.305	1.108	HYP
	0.4	2.47	0.387	0.480	13.73	0.226	1.839	0.874	0.193	3.059	1.455	1.247	2.648	1.471	1.249	HYP
	0.5	1.34	0.361	0.547	16.43	0.241	1.888	0.923	0.159	2.983	1.419	1.217	2.619	1.455	1.236	HYP
B	0.4	0.94	0.010	1.000	20.65	0.327	1.988	1.026	0.217	5.238	2.492	2.136	4.490	2.494	2.118	OBE
	0.5	0.98	0.010	1.000	19.10	0.317	2.335	1.009	0.212	4.699	2.235	1.916	4.054	2.252	1.912	OBE
C	0.6	1.01	0.010	1.000	18.010	0.306	2.705	0.991	0.207	4.297	2.044	1.752	3.728	2.071	1.758	OBE
	0.7	1.05	0.010	1.000	17.040	0.295	3.132	0.970	0.203	3.983	1.895	1.624	3.467	1.926	1.636	HYP
	0.8	1.09	0.010	1.000	16.230	0.284	3.598	0.949	0.201	3.732	1.775	1.522	3.257	1.809	1.536	HYP
	0.9	1.14	0.010	1.000	15.490	0.273	4.127	0.926	0.199	3.526	1.678	1.438	3.083	1.712	1.454	HYP
	1.0	1.19	0.010	1.000	14.870	0.262	4.699	0.902	0.198	3.356	1.597	1.369	2.937	1.632	1.386	HYP
	1.5	1.47	0.010	0.990	12.720	0.210	8.329	0.788	0.195	2.828	1.345	1.153	2.478	1.377	1.169	HYP

TABLE VI.   The columns list the same quantities as in Table V but for the HFO EOS.

Type	$\hat{A}^{-1}$	ϵ_{max}	$\frac{r_p}{r_e}$	$\hat{\beta}$	R_c	$\frac{T}{|W|}$	$\frac{\Omega_c}{\Omega_e}$	$\frac{J}{M^2}$	C	$\frac{M_0}{M_\odot}$	$\frac{M_0}{M_{0,max}^{TOV}}$	$\frac{M_0}{M_{0,max}^{sup}}$	$\frac{M_{ADM}}{M_\odot}$	$\frac{M_{ADM}}{M_{ADM,max}^{TOV}}$	$\frac{M_{ADM}}{M_{ADM,max}^{sup}}$	CLASS
A	0.0	2.32	0.564	0.078	13.710	0.125	1.000	0.677	0.178	2.829	1.174	1.000	2.440	1.187	1.000	SUP
	0.1	2.32	0.550	0.089	13.810	0.132	1.054	0.695	0.179	2.863	1.188	1.012	2.470	1.202	1.012	HYP
	0.2	2.30	0.515	0.207	14.040	0.153	1.214	0.746	0.183	2.972	1.234	1.051	2.567	1.249	1.052	HYP
	0.3	2.24	0.450	0.334	14.470	0.192	1.496	0.820	0.191	3.199	1.328	1.131	2.767	1.346	1.134	HYP
	0.4	1.54	0.376	0.565	15.690	0.245	1.869	0.900	0.200	3.624	1.504	1.281	3.134	1.525	1.284	HYP
	0.5	0.99	0.360	0.544	18.320	0.242	1.841	0.935	0.154	3.177	1.319	1.123	2.817	1.370	1.154	HYP
B	0.4	0.80	0.011	0.999	21.960	0.327	2.025	1.020	0.221	5.642	2.342	1.994	4.854	2.362	1.989	OBE
	0.5	0.83	0.010	1.000	20.380	0.316	2.378	1.002	0.215	5.070	2.105	1.792	4.391	2.136	1.800	OBE
C	0.6	0.86	0.010	1.000	19.150	0.305	2.772	0.983	0.211	4.644	1.928	1.642	4.041	1.966	1.656	HYP
	0.7	0.90	0.010	1.000	18.060	0.293	3.231	0.960	0.208	4.312	1.790	1.524	3.763	1.831	1.542	HYP
	0.8	0.94	0.010	1.000	17.160	0.282	3.734	0.937	0.206	4.048	1.680	1.431	3.539	1.722	1.450	HYP
	0.9	0.99	0.010	1.000	16.330	0.270	4.314	0.911	0.205	3.833	1.591	1.355	3.355	1.632	1.375	HYP
	1.0	1.03	0.010	1.000	15.710	0.258	4.913	0.887	0.204	3.657	1.518	1.293	3.204	1.559	1.313	HYP
	1.5	1.29	0.010	1.000	13.440	0.203	8.863	0.769	0.203	3.120	1.295	1.103	2.732	1.329	1.120	HYP

considered here, the maximum rest mass model is the configuration with $\hat{A}^{-1} = 0.4$ (the lowest value of $\hat{A}^{-1}$ for which Type B models exist that we considered) and is always an overmassive Type B model. For polytropes, Ref. [20] showed that Type B models at the lowest possible value of $\hat{A}^{-1}$ are the most massive ones, too. As shown in Tables V–VIII, depending on the EOS overmassive configurations arise not only for Type B, but also for Type C stars. Our search results suggest that OMNSs are, in general, more common for softer EOSs, which is consistent with our finding that softer EOSs lead to larger increases in the rest mass.

We now compare our results for the APR and FPS EOSs with those of [17]. In [17] models of differentially rotating stars were constructed that exceeded the TOV limit rest mass by at most 31% for APR and 46% for FPS. Given that the maximum rest mass models for APR and FPS reported in [17] correspond to $\hat{A}^{-1} = 0.3$ and $\hat{A}^{-1} = 0.5$, respectively, it suggests that these models were of Type A. However, maximum rest mass Type B models (quasitoroidal models at a low degree of differential rotation) are in all cases more massive than maximum rest mass Type A and C models. When considering Type B models, we find that the maximum rest mass can increase by as much as approximately 100% and 150% in the cases of APR and FPS, respectively. The largest increase in rest mass for NL3 and HFO is approximately 120% and 130%, respectively. These maximum rest mass configurations are all OMNSs. We emphasize the fact that generally Type B models tend to be the most massive and that they show the largest increase in rest mass when compared to the TOV limit, as depicted in Fig. 5.

TABLE VII.   The columns list the same quantities as in Table V but for the NL3 EOS.

Type	$\hat{A}^{-1}$	ϵ_{max}	$\frac{r_p}{r_e}$	$\hat{\beta}$	R_c	$\frac{T}{|W|}$	$\frac{\Omega_c}{\Omega_e}$	$\frac{J}{M^2}$	C	$\frac{M_0}{M_\odot}$	$\frac{M_0}{M_{0,max}^{TOV}}$	$\frac{M_0}{M_{0,max}^{sup}}$	$\frac{M_{ADM}}{M_\odot}$	$\frac{M_{ADM}}{M_{ADM,max}^{TOV}}$	$\frac{M_{ADM}}{M_{ADM,max}^{sup}}$	CLASS
A	0.0	1.36	0.559	0.064	17.490	0.136	1.000	0.704	0.189	3.881	1.185	1.000	3.301	1.202	1.000	SUP
	0.1	1.36	0.540	0.080	17.690	0.145	1.062	0.726	0.190	3.940	1.203	1.015	3.353	1.221	1.016	HYP
	0.2	1.34	0.498	0.226	18.020	0.172	1.248	0.784	0.196	4.134	1.263	1.065	3.524	1.283	1.067	HYP
	0.3	1.24	0.411	0.395	18.780	0.225	1.603	0.872	0.209	4.598	1.405	1.185	3.925	1.429	1.189	HYP
	0.4	0.72	0.365	0.502	21.920	0.248	1.736	0.921	0.182	4.609	1.408	1.188	3.984	1.450	1.207	HYP
	0.5	0.54	0.359	0.521	23.820	0.242	1.754	0.957	0.141	3.777	1.154	0.973	3.367	1.226	1.020	HYP
B	0.4	0.50	0.010	1.000	27.180	0.326	2.050	1.016	0.224	7.114	2.173	1.833	6.082	2.214	1.842	OBE
	0.5	0.52	0.010	1.000	25.180	0.315	2.419	0.996	0.219	6.403	1.956	1.650	5.508	2.005	1.668	HYP
C	0.6	0.54	0.010	1.000	23.630	0.303	2.833	0.975	0.215	5.875	1.795	1.514	5.075	1.847	1.537	HYP
	0.7	0.57	0.010	1.000	22.140	0.290	3.342	0.948	0.214	5.468	1.670	1.409	4.731	1.722	1.433	HYP
	0.8	0.60	0.010	1.000	20.960	0.278	3.901	0.922	0.213	5.147	1.572	1.326	4.458	1.623	1.350	HYP
	0.9	0.63	0.010	1.000	19.980	0.265	4.515	0.895	0.212	4.889	1.493	1.260	4.237	1.542	1.283	HYP
	1.0	0.66	0.010	1.000	19.170	0.252	5.184	0.869	0.212	4.679	1.429	1.206	4.056	1.477	1.229	HYP
	1.5	0.83	0.010	1.000	16.500	0.193	9.511	0.746	0.213	4.059	1.240	1.046	3.509	1.277	1.063	HYP

TABLE VIII.   The columns list the same quantities as in Table V but for the APR EOS.

Type	$\hat{A}^{-1}$	ϵ_{max}	$\frac{r_p}{r_e}$	$\hat{\beta}$	R_c	$\frac{T}{|W|}$	$\frac{\Omega_c}{\Omega_e}$	$\frac{J}{M^2}$	C	$\frac{M_0}{M_\odot}$	$\frac{M_0}{M^{TOV}_{0,max}}$	$\frac{M_0}{M^{sup}_{0,max}}$	$\frac{M_{ADM}}{M_\odot}$	$\frac{M_{ADM}}{M^{TOV}_{ADM,max}}$	$\frac{M_{ADM}}{M^{sup}_{ADM,max}}$	CLASS
A	0.0	2.42	0.564	0.059	12.900	0.137	1.000	0.709	0.201	3.091	1.163	1.000	2.599	1.187	1.000	SUP
	0.1	2.43	0.546	0.121	12.980	0.148	1.074	0.735	0.204	3.141	1.182	1.016	2.644	1.208	1.017	HYP
	0.2	2.41	0.490	0.248	13.270	0.181	1.298	0.801	0.210	3.306	1.244	1.070	2.793	1.276	1.075	HYP
	0.3	2.00	0.414	0.508	13.700	0.236	1.703	0.880	0.226	3.649	1.373	1.181	3.095	1.414	1.191	HYP
	0.4	1.27	0.368	0.510	16.360	0.247	1.769	0.912	0.186	3.547	1.335	1.148	3.047	1.392	1.172	HYP
	0.5	0.99	0.377	0.521	17.520	0.231	1.772	0.925	0.144	2.852	1.073	0.923	2.525	1.154	0.972	HYP
B	0.4	0.86	0.011	1.000	20.900	0.327	2.025	1.020	0.221	5.410	2.036	1.751	4.621	2.111	1.778	OBE
	0.5	0.91	0.010	1.000	19.090	0.315	2.432	0.996	0.219	4.875	1.835	1.578	4.182	1.910	1.609	HYP
C	0.6	0.95	0.010	1.000	17.830	0.304	2.869	0.973	0.216	4.476	1.685	1.448	3.853	1.760	1.483	HYP
	0.7	0.99	0.010	1.000	16.830	0.291	3.353	0.949	0.214	4.168	1.569	1.349	3.597	1.643	1.384	HYP
	0.8	1.04	0.010	1.000	15.920	0.279	3.918	0.922	0.213	3.926	1.477	1.270	3.391	1.549	1.305	HYP
	0.9	1.10	0.010	1.000	15.110	0.265	4.572	0.894	0.213	3.732	1.405	1.208	3.223	1.472	1.240	HYP
	1.0	1.16	0.010	1.000	14.440	0.252	5.285	0.866	0.214	3.576	1.346	1.157	3.087	1.410	1.188	HYP
	1.5	1.48	0.010	1.000	12.340	0.190	9.915	0.739	0.217	3.124	1.176	1.011	2.683	1.226	1.032	HYP

We find that among Type A models, those with larger values of $\hat{A}^{-1}$ tend to have a larger rest mass. However, the relationship between $\hat{A}^{-1}$ and M_0 for Type A models is not monotonic. There appears to be a value of $\hat{A}^{-1}$ above which the maximum rest mass begins to decrease as seen from the curves in the lower left corner of Fig. 5. This feature of the solution space was also observed in [21] for a $\Gamma = 2.5$ polytrope, suggesting that it may arise for stiffer EOSs. We note that this feature is observed for all EOSs we study here, which have effective polytropic exponents of $\Gamma^{nuc}_{eff} \gtrsim 2.5$. For Type A the largest rest mass models were found for values of $\hat{A}^{-1}$ of 0.35 for both APR and NL3, 0.4 for HFO, and 0.45 for FPS, suggesting that the value of $\hat{A}^{-1}$ at which the maximum rest mass begins to decrease is smaller for stiffer EOSs (note that we also built maximum rest mass Type A models in increments of $\hat{A}^{-1} = 0.05$ for finer resolution in Fig. 5).

For Type B and C models, we observe the same monotonic behavior between the increase in rest mass relative to the TOV limit and $\hat{A}^{-1}$ as seen for stiffer EOSs in [21]; i.e., the maximum rest mass increases with decreasing $\hat{A}^{-1}$. We also find the same general ordering of EOS by stiffness whereby softer EOSs (FPS and HFO) tend to exhibit larger increases of the rest mass compared to the TOV limit (see Fig. 5).

It is noteworthy that the largest increase in rest mass is seen in the FPS EOS, the softest EOS in our set. In [21] the maximal increase in rest mass was observed for a moderately stiff EOS, which was neither the softest nor the stiffest considered. There it was argued that, generally, the increase in rest mass compared to the TOV limit due to differential rotation decreases with increasing stiffness. We observe the same trend with realistic EOSs for Type B and C models, which indicates that the largest increase in rest mass due to differential rotation is possible for quasitoroidal configurations described by softer EOSs. For the polytropes

considered in [21], it was found that stiffer EOSs show larger increases in the rest mass for Type A models of *low* $\hat{A}^{-1}$ (0.0 to 0.4) We find a similar general trend for the Type A models at low $\hat{A}^{-1}$ (0.0 to 0.3) presented here. However, an "anomaly" in this trend is seen in the case of the APR EOS. For instance, the low $\hat{A}^{-1}$ (0.0 to 0.3) maximum rest mass models for the FPS EOS (the softest considered here) show a very similar increase in the rest mass as those of APR (the stiffest EOS considered here), as can be seen from
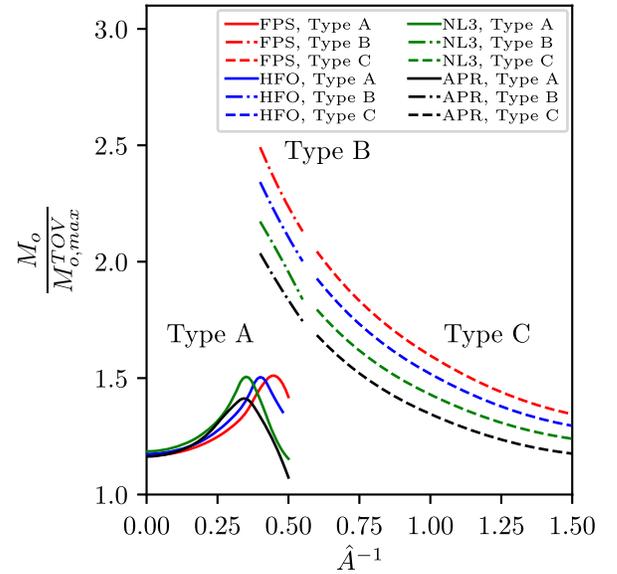
FIG. 5.   Ratio of rest mass M_0 to maximum TOV rest mass $M^{TOV}_{0,max}$ as a function of degree of differential rotation $\hat{A}^{-1}$ for each solution type and EOS. The solid lines show the relative increase for Type A models, the dash-dotted lines show the relative increase for Type B models, and the dashed lines show the relative increase for Type C models. The red, blue, green, and black lines correspond to the FPS, HFO, NL3, and APR EOSs, respectively.

the low $\hat{A}^{-1}$ part of the leftmost curves of Fig. 5 and the corresponding $\frac{M_0}{M_{0,\max}^{\mathrm{TOV}}}$ entries of Tables V and VIII for Type A models of low $\hat{A}^{-1}$. A possible explanation for the break in the trend is that the authors of [21] consider a large range of adiabatic indices $1.8 \leq \Gamma \leq 3.0$, whereas the effective adiabatic indices of the EOSs in our sample cover a smaller range. On the other hand, assigning one number to stiffness in the case of realistic EOSs may not be entirely appropriate as the stiffness defined through stellar models may depend on the choice of mass. For example, the TOV mass-radius curves of the HFO and APR EOSs intersect near their corresponding TOV limits (see Appendix C). In this work we defined stiffness based on the maximum rest mass TOV configurations and on TOV configurations with a gravitational mass of $1.4\,M_\odot$. It is also the case that Type A configurations of low $\hat{A}^{-1}$ mostly sample the value of $\epsilon_{\max}$ from higher density regions of the EOSs which may be of comparable stiffness. This is supported by the fact that in all cases considered here, the values of $\epsilon_{\max}$ for the Type A models of low $\hat{A}^{-1}$ are larger than for the Type B and C models. The anomaly we mentioned above would not be observed for EOSs of constant stiffness as defined by the effective polytropic exponent, as in the case of the polytropes of the fixed polytropic index studied in [21]. A systematic study of the effect may employ realistic EOSs as done here or a piecewise polytropic EOS such as those presented in [29–31], where the polytropic index has a dependence on the energy density. However, such a study goes beyond the scope of the current work.

VI. CONCLUSIONS AND DISCUSSION

In this paper, we have presented results for the solution space of general relativistic differentially rotating neutron stars with realistic EOSs. We found that the different types of differentially rotating equilibrium solutions that were previously discovered for polytropes [20,21] with the KEH rotation law [18] exist for realistic neutron star equations of state, too. Moreover, we demonstrated that codes based on the KEH scheme [18], such as the Cook code [22,28], can build these different types of stars, although we were not able to construct Type D sequences of constant degree of differential rotation and constant maximum energy density or complete Type B sequences. The Cook code is capable of building most of the extremely massive quasitoroidal, relativistic configurations using realistic EOSs, but finds it challenging to converge on solutions that are both highly pinched and quasitoroidal. Note that Type D stars are not likely to be physical [20,21].

We presented the maximum rest mass configurations found in our search of the solution space for three of the four types of solutions we were able to construct. As in [20,21] we find configurations that can support a mass more than 2 times the TOV limit. We called these configurations overmassive. For the equations of state

considered here we find that overmassive stars can support up to 150% more rest mass than the TOV limit mass with the same equation of state. This number is a lower limit to the maximum rest mass that can be supported by differential rotation. We have classified the maximum mass configurations we found as supramassive, hypermassive, or overmassive, and we found that depending on the equation of state overmassive stars can be Type B or Type C.

Differentially rotating hypermassive neutron stars can form following binary neutron star mergers. Clearly, following such a merger, the remnant configuration cannot have mass more than 2 times the TOV limit mass. Thus, the overmassive configurations we found may never appear in nature, and if they do, they would have to form through some more exotic channel. Moreover, it is well known that in binary neutron star mergers there exists a threshold value for the binary total mass above which a black hole forms promptly after merger [32–37]. This value for the threshold mass (M_{thres}) depends on the equation of state, and for quasicircular, irrotational binaries it may be up to ∼70% greater than the TOV limit mass [32]. It may also be that for irrotational binaries $M_{\mathrm{thres}} \in [2.75 - 3.25]M_\odot$ [38]. Therefore, it may be difficult to form even extreme hypermassive neutron stars in binary neutron star mergers. An exception may be dynamical capture mergers such as those studied recently in [39–46], where the total angular momentum at merger can be higher than those in quasicircular binaries, which can provide additional centrifugal support.

Regardless of the precise value of M_{thres} the question about what type of differentially rotating star can form following a neutron star merger remains open. This is interesting because less dramatic, but significant, increases to the maximum supportable mass can arise for degrees of differential rotation different from those corresponding to the more extreme cases. Such configurations may be relevant for binary neutron star mergers and may have implications for the stability and lifetime of their hypermassive neutron star remnants.

Another important question is how well the KEH rotation law describes the differential rotation profile of a hypermassive neutron star formed in a binary neutron star merger and whether the different types of stellar solutions are unique to the KEH law. The rotational properties of hypermassive neutron stars formed in quasicircular binary neutron star mergers have been studied recently in a number of works [47–51], and they appear to deviate from that of the KEH rotation law. Nevertheless, the rotation profiles reported in [41,42] for eccentric neutron star mergers are different and seem to be within the realm of the KEH rotation law. Interestingly, the remnants found in [41,42] were also quasitoroidal. In a recent work a new differential rotation law was introduced [52] that captures the rotational profile of some binary neutron star merger remnants. An interesting follow-up to our work is to adopt this new rotation law and investigate the maximum possible mass that can be supported

for different realistic EOSs and whether different types (or even more types) of differentially rotating stars arise.

Finally, the issue of dynamical stability of the different types of differentially rotating stars is important to address. Moreover, are overmassive stars dynamically stable? Many of the equilibrium configurations we built have $T/|W| > 0.25$, and hence are unstable to a dynamical bar mode instability (see [7] and references therein). Some of the configurations we built have dimensionless spin parameter $J/M^2 > 1$, which does not necessarily imply collapse on a secular timescale, as the star can be unstable to nonaxisymmetric modes and collapse through fragmentation (see [7,53,54] for a review). Nonaxisymmetric instabilities in differentially rotating stars arise even for low values of $T/|W|$ [55–63] and in binary neutron star merger remnants [41–43,64,65]. If a certain type of solution is dynamically unstable to collapse, then it cannot arise in nature, despite the fact that the equilibrium configuration can support an amount of mass much larger than the TOV limit. Unlike the case of uniformly rotating stars the turning point theorem [66–68] does not apply to differentially rotating stars (although it seems to apply approximately for Type A configurations [69,70]); therefore dynamical simulations in full general relativity offer a straightforward avenue to study the dynamical stability of these configurations. The solutions we have constructed can serve as initial data for such dynamical simulations. We will address all of these open questions in future studies.

ACKNOWLEDGMENTS

APPENDIX A: CALCULATION OF POLYTROPIC REPRESENTATION OF REALISTIC EQUATIONS OF STATE

When building polytropic stellar configurations in geometrized units, the polytropic constant κ defines a fundamental length scale ($\kappa^{n/2}$), which scales out of the problem. To calculate $\kappa_{\text{eff}}^{\text{nuc}}$ we first build the maximum rest mass TOV models for polytropes with $\Gamma_{\text{eff}}^{\text{nuc}}$ as defined in Eq. (9). Next, we calculate the polytropic constant in geometrized units $\kappa_{\text{eff,geo}}^{\text{nuc}}$ by matching the maximum TOV ADM masses of the nuclear and polytropic EOSs,

$$\kappa_{\text{eff,geo}}^{\text{nuc}} = \left(\frac{M_{\text{ADM,max}}^{\text{TOV,nuc}}}{M_{\text{ADM,max}}^{\text{TOV,poly}}}\right)^{\frac{2}{n_{\text{eff}}^{\text{nuc}}}}. \tag{A1}$$

The quantity in the parentheses of Eq. (A1) is then converted to a unit of length (specifically, we work in cgs units). We then replace the appropriate factors of G and c needed to express our physical quantities in cgs units,

$$\kappa_{\text{eff}}^{\text{nuc}} = \frac{G^{\frac{1}{n}}}{c^{\frac{2}{n}-2}}\kappa_{\text{eff,geo}}^{\text{nuc}}. \tag{A2}$$

Finally, we write the polytropic representation of the nuclear EOSs we considered as

$$P = \kappa_{\text{eff}}^{\text{nuc}}\rho_0^{\Gamma_{\text{eff}}^{\text{nuc}}} \tag{A3}$$

and

$$\epsilon = \rho_0 c^2 + \frac{P}{(\Gamma_{\text{eff}}^{\text{nuc}} - 1)}, \tag{A4}$$

where $\Gamma_{\text{eff}}^{\text{nuc}}$ is the effective adiabatic index as calculated in Sec. III.

APPENDIX B: C_ϵ AS A MEASURE OF EOS STIFFNESS

Here we discuss how C_ϵ as defined through Eqs. (7) and (8) varies with rest mass and how that may change the ranking of EOS stiffness. In Fig. 6, we present the ratio of average energy density to maximum energy density (C_ϵ) plotted against the rest mass for the TOV sequence of each EOS we treat in this paper. As can be seen from Fig. 6, the value of C_ϵ changes as a function of the rest mass M_0, so that depending on the choice of M_0 the EOS ranking by stiffness based solely on C_ϵ may change. However, since
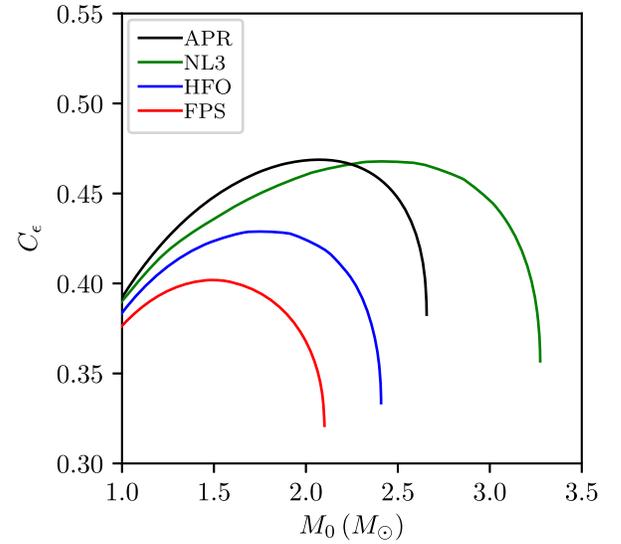
FIG. 6. Ratio of average energy density to maximum energy density C_ϵ as a function of rest mass along the TOV sequence for each EOS in our study.

the stiffness comparison is at fixed rest mass, the EOS ranking by stiffness remains unchanged (and is the one we list in Table I), if we cap the range of masses at the maximum mass of the FPS EOS.

Nevertheless, C_{ϵ} should not be adopted as the *definitive* measure of EOS stiffness for realistic EOSs. This is why we also considered $\Gamma_{\mathrm{eff}}^{\mathrm{nuc}}$ as calculated in Sec. III. By both measures of the stiffness, the ranking of EOS by stiffness is consistent with the one presented in Table I.

APPENDIX C: MASS-RADIUS CURVES FOR REALISTIC EQUATIONS OF STATE

Here we present the mass-radius relation of the nuclear equations of state used in this work. As can be seen from Fig. 7, all EOSs but the FPS EOS respect the upper bound set on NS masses from observations of the most massive pulsar to date, PSR J1614-2230 [72,73]. Despite the FPS EOS having a maximum mass that falls below this upper bound we include it in this study to offer a comparison to the results of [17]. It is also useful to consider the FPS EOS as an example of a relatively soft nuclear EOS. We find that the maximum increase in rest mass when compared to the TOV mass for the FPS EOS is the highest (150%) in the set of EOS we considered (see Fig. 5), which is consistent with our finding that softer EOSs result in larger increases of the rest mass relative to the TOV mass.

All EOSs but the NL3 EOS respect the 90% confidence upper bound on NS radii set by the tidal deformability of NSs as inferred from GW170817 [12,74,75]. The NL3 EOS may also have too high a maximum mass [8–10,76]. Despite the fact that using the NL3 EOS results in stars with masses and radii above these bounds, we include it in this study to investigate the solution space of differentially rotating stars and maximum rest mass solutions for an EOS
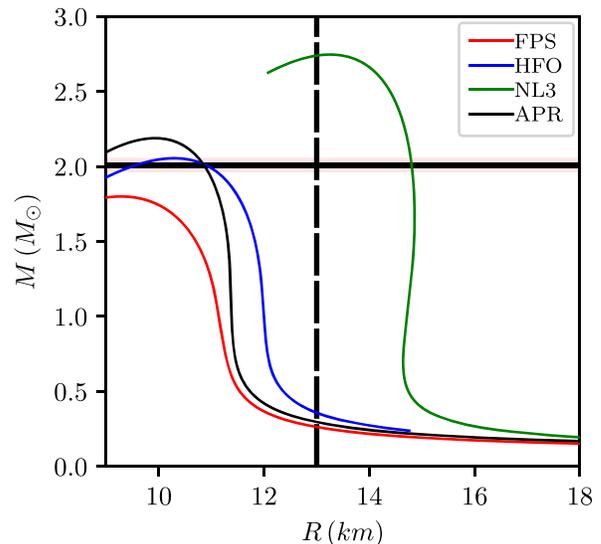
FIG. 7. Mass-radius relation for the realistic EOSs used in this work. The red, blue, green, and black lines correspond to the FPS, HFO, NL3, and APR EOSs, respectively. The solid horizontal line and red horizontal band correspond to the upper bound on the NS mass from observations of PSR J1614-2230 [72]. The vertical solid line corresponds to the upper limit on the NS radius from considerations of the tidal deformability as inferred from GW170817 [74].

with a relatively large TOV mass. It is also useful to consider the NL3 EOS to investigate the solution space of differentially rotating stars for a relatively stiff EOS. We find that the maximum increase in rest mass when compared to the TOV mass for the NL3 EOS is among the lowest (120%) in the set of EOSs we considered, which is consistent with our finding that stiffer EOSs result in smaller increases of the rest mass relative to the TOV mass.

[1] T. W. Baumgarte, S. L. Shapiro, and M. Shibata, Astrophys. J. Lett. **528,** L29 (2000).

[2] Y. Sekiguchi, K. Kiuchi, K. Kyutoku, and M. Shibata, Phys. Rev. Lett. **107,** 051102 (2011).

[3] V. Paschalidis, Z. B. Etienne, and S. L. Shapiro, Phys. Rev. D **86,** 064032 (2012).

[4] J. A. Faber and F. A. Rasio, Living Rev. Relativity **15,** 8 (2012).

[5] V. Paschalidis, Classical Quantum Gravity **34,** 084002 (2017).

[6] L. Baiotti and L. Rezzolla, Rep. Prog. Phys. **80,** 096901 (2017).

[7] V. Paschalidis and N. Stergioulas, Living Rev. Relativity **20,** 7 (2017).

[8] M. Shibata, S. Fujibayashi, K. Hotokezaka, K. Kiuchi, K. Kyutoku, Y. Sekiguchi, and M. Tanaka, Phys. Rev. D **96,** 123012 (2017).

[9] B. Margalit and B. D. Metzger, Astrophys. J. Lett. **850,** L19 (2017).

[10] M. Ruiz, S. L. Shapiro, and A. Tsokaros, Phys. Rev. D **97,** 021501 (2018).

[11] X. Zhang and Z. Cao, Int. J. Mod. Phys. D **28,** 1950026 (2019).

[12] B. P. Abbott *et al.* (Virgo and LIGO Scientific Collaborations), Phys. Rev. Lett. **119,** 161101 (2017).

[13] B. P. Abbott *et al.*, Astrophys. J. Lett. **848,** L12 (2017).

[14] M. D. Duez, Y. T. Liu, S. L. Shapiro, M. Shibata, and B. C. Stephens, Phys. Rev. Lett. **96,** 031101 (2006).

[15] M. D. Duez, Y. T. Liu, S. L. Shapiro, M. Shibata, and B. C. Stephens, Phys. Rev. D **73,** 104015 (2006).

[16] N. D. Lyford, T. W. Baumgarte, and S. L. Shapiro, Astrophys. J. **583,** 410 (2003).

[17] I. A. Morrison, T. W. Baumgarte, and S. L. Shapiro, Astrophys. J. **610,** 941 (2004).

[18] H. Komatsu, Y. Eriguchi, and I. Hachisu, Mon. Not. R. Astron. Soc. **237,** 355 (1989).

[19] M. Ansorg, D. Gondek-Rosinska, and L. Villain, Mon. Not. R. Astron. Soc. **396,** 2359 (2009).

[20] D. Gondek-Rosinska, I. Kowalska, L. Villain, M. Ansorg, and M. Kucaba, Astrophys. J. **837,** 58 (2017).

[21] A. M. Studzinska, M. Kucaba, D. Gondek-Rosinska, L. Villain, and M. Ansorg, Mon. Not. R. Astron. Soc. **463,** 2667 (2016).

[22] G. Cook, S. Shapiro, and S. Teukolsky, Astrophys. J. **422,** 227 (1994).

[23] S. Typel, M. Oertel, and T. Klhn, Phys. Part. Nucl. **46,** 633 (2015).

[24] A. Akmal, V. R. Pandharipande, and D. G. Ravenhall, Phys. Rev. C **58,** 1804 (1998).

[25] C. P. Lorenz, D. G. Ravenhall, and C. J. Pethick, Phys. Rev. Lett. **70,** 379 (1993).

[26] G. Shen, C. J. Horowitz, and S. Teige, Phys. Rev. C **83,** 035802 (2011).

[27] M. Hempel and J. Schaffner-Bielich, Nucl. Phys. **A837,** 210 (2010).

[28] G. Cook, S. Shapiro, and S. Teukolsky, Astrophys. J. **424,** 823 (1994).

[29] J. S. Read, B. D. Lackey, B. J. Owen, and J. L. Friedman, Phys. Rev. D **79,** 124032 (2009).

[30] F. Ozel and D. Psaltis, Phys. Rev. D **80,** 103003 (2009).

[31] C. A. Raithel, F. Ozel, and D. Psaltis, Astrophys. J. **831,** 44 (2016).

[32] M. Shibata and K. Taniguchi, Phys. Rev. D **73,** 064027 (2006).

[33] M. Shibata, K. Taniguchi, and K. Uryū, Phys. Rev. D **68,** 084020 (2003).

[34] M. Shibata, K. Taniguchi, and K. Uryū, Phys. Rev. D **71,** 084021 (2005).

[35] K. Hotokezaka, K. Kyutoku, H. Okawa, M. Shibata, and K. Kiuchi, Phys. Rev. D **83,** 124008 (2011).

[36] A. Bauswein, T. W. Baumgarte, and H. T. Janka, Phys. Rev. Lett. **111,** 131101 (2013).

[37] A. Bauswein and N. Stergioulas, Mon. Not. R. Astron. Soc. **471,** 4956 (2017).

[38] V. Paschalidis and M. Ruiz, arXiv:1808.04822.

[39] R. Gold, S. Bernuzzi, M. Thierfelder, B. Brugmann, and F. Pretorius, Phys. Rev. D **86,** 121501 (2012).

[40] W. E. East and F. Pretorius, Astrophys. J. **760,** L4 (2012).

[41] V. Paschalidis, W. E. East, F. Pretorius, and S. L. Shapiro, Phys. Rev. D **92,** 121502 (2015).

[42] W. E. East, V. Paschalidis, F. Pretorius, and S. L. Shapiro, Phys. Rev. D **93,** 024011 (2016).

[43] W. E. East, V. Paschalidis, and F. Pretorius, Classical Quantum Gravity **33,** 244004 (2016).

[44] D. Radice, F. Galeazzi, J. Lippuner, L. F. Roberts, C. D. Ott, and L. Rezzolla, Mon. Not. R. Astron. Soc. **460,** 3255 (2016).

[45] S. V. Chaurasia, T. Dietrich, N. K. Johnson-McDaniel, M. Ujevic, W. Tichy, and B. Brgmann, Phys. Rev. D **98,** 104005 (2018).

[46] L. J. Papenfort, R. Gold, and L. Rezzolla, Phys. Rev. D **98,** 104028 (2018).

[47] W. Kastaun and F. Galeazzi, Phys. Rev. D **91,** 064027 (2015).

[48] W. Kastaun, R. Ciolfi, and B. Giacomazzo, Phys. Rev. D **94,** 044060 (2016).

[49] W. Kastaun, R. Ciolfi, A. Endrizzi, and B. Giacomazzo, Phys. Rev. D **96,** 043019 (2017).

[50] M. Hanauske, K. Takami, L. Bovard, L. Rezzolla, J. A. Font, F. Galeazzi, and H. Stöcker, Phys. Rev. D **96,** 043004 (2017).

[51] R. Ciolfi, W. Kastaun, B. Giacomazzo, A. Endrizzi, D. M. Siegel, and R. Perna, Phys. Rev. D **95,** 063016 (2017).

[52] K. Uryu, A. Tsokaros, L. Baiotti, F. Galeazzi, K. Taniguchi, and S. Yoshida, Phys. Rev. D **96,** 103011 (2017).

[53] B. Zink, N. Stergioulas, I. Hawke, C. D. Ott, E. Schnetter, and E. Mueller, Phys. Rev. D **76,** 024019 (2007).

[54] C. Reisswig, C. D. Ott, E. Abdikamalov, R. Haas, P. Moesta, and E. Schnetter, Phys. Rev. Lett. **111,** 151101 (2013).

[55] J. M. Centrella, K. C. B. New, L. L. Lowe, and J. D. Brown, Astrophys. J. Lett. **550,** L193 (2001).

[56] M. Saijo, T. W. Baumgarte, and S. L. Shapiro, Astrophys. J. **595,** 352 (2003).

[57] A. L. Watts, N. Andersson, and D. I. Jones, Astrophys. J. Lett. **618,** L37 (2005).

[58] M. Saijo and S. Yoshida, Mon. Not. R. Astron. Soc. **368,** 1429 (2006).

[59] S. Ou and J. E. Tohline, Astrophys. J. **651,** 1068 (2006).

[60] G. Corvino, L. Rezzolla, S. Bernuzzi, R. De Pietri, and B. Giacomazzo, Classical Quantum Gravity **27,** 114104 (2010).

[61] M. Saijo and S. Yoshida, Phys. Rev. D **94,** 084032 (2016).

[62] S. Yoshida and M. Saijo, Mon. Not. R. Astron. Soc. **466,** 600 (2017).

[63] M. Saijo, Phys. Rev. D **98,** 024003 (2018).

[64] D. Radice, S. Bernuzzi, and C. D. Ott, Phys. Rev. D **94,** 064011 (2016).

[65] L. Lehner, S. L. Liebling, C. Palenzuela, and P. M. Motl, Phys. Rev. D **94,** 043003 (2016).

[66] R. Sorkin, Astrophys. J. **249,** 254 (1981).

[67] J. L. Friedman, J. R. Ipser, and R. D. Sorkin, Astrophys. J. **325,** 722 (1988).

[68] J. S. Schiffrin and R. M. Wald, Classical Quantum Gravity **31,** 035024 (2014).

[69] L. R. Weih, E. R. Most, and L. Rezzolla, Mon. Not. R. Astron. Soc. **473,** L126 (2018).

[70] G. Bozzola, N. Stergioulas, and A. Bauswein, Mon. Not. R. Astron. Soc. **474,** 3557 (2018).

[71] N. Stergioulas and J. Friedman, Astrophys. J. **444,** 306 (1995).

[72] P. B. Demorest, T. Pennucci, S. M. Ransom, M. S. E. Roberts, and J. W. T. Hessels, Nature (London) **467,** 1081 (2010).

[73] J. Antoniadis et al., Science **340,** 1233232 (2013).

[74] C. Raithel, F. Özel, and D. Psaltis, Astrophys. J. **857,** L23 (2018).

[75] B. P. Abbott et al. (Virgo and LIGO Scientific Collaborations), Phys. Rev. Lett. **121,** 161101 (2018).

[76] L. Rezzolla, E. R. Most, and L. R. Weih, Astrophys. J. **852,** L25 (2018).